Calcif Tissue Int
DOI 10.1007/s00223-008-9174-x

Bone Volume Fraction Explains the Variation in Strength and Stiffness of Cancellous Bone Affected by Metastatic Cancer and Osteoporosis

Ara Nazarian · Dietrich von Stechow · David Zurakowski · Ralph Müller · Brian D. Snyder

Received: 5 June 2008 / Accepted: 25 August 2008

Abstract Preventing nontraumatic fractures in millions of patients with osteoporosis or metastatic cancer may significantly reduce the associated morbidity and reduce health-care expenditures incurred by these fractures. Predicting fracture occurrence requires an accurate understanding of the relationship between bone structure and the mechanical properties governing bone fracture that can be readily measured. The aim of this study was to test the hypothesis that a single analytic relationship with either bone tissue mineral density or bone volume fraction (BV/TV) as independent variables could predict the strength and stiffness of normal and pathologic cancellous bone affected by osteoporosis or metastatic cancer. After obtaining institutional review board approval and informed consent, 15 patients underwent excisional biopsy of metastatic prostate, breast, lung, ovarian, or colon cancer from the spine and/or femur to obtain 41 metastatic cancer specimens. In addition, 96 noncancer specimens were excised from 43 age- and site-matched cadavers. All specimens were imaged using micro-computed tomography (micro-CT) and backscatter emission imaging and tested mechanically by uniaxial compression and nanoindentation. The minimum BV/TV, measured using quantitative micro-CT, accounted for 84% of the variation in bone stiffness and strength for all cancellous bone specimens. While relationships relating bone density to strength and stiffness have been derived empirically for normal and osteoporotic bone, these relationships have not been applied to skeletal metastases. This simple analytic relationship will facilitate large-scale screening and prediction of fracture risk for normal and pathologic cancellous bone using clinical CT systems to determine the load capacity of bones altered by metastatic cancer, osteoporosis, or both.

Keywords Osteoporosis · Skeletal metastasis · Cancellous bone · Mechanical property · Bone volume fraction · Bone mineral density

A. Nazarian · D. von Stechow · B. D. Snyder
Orthopedic Biomechanics Laboratory, Beth Israel Deaconess Medical Center, Harvard Medical School, Boston, MA 02215, USA

A. Nazarian
Institute for Biomedical Engineering, University and ETH Zürich, Zürich 8044, Switzerland
e-mail: anazaria@bidmc.harvard.edu

R. Müller
Institute for Biomechanics, ETH Zürich, Zürich 8044, Switzerland

D. Zurakowski · B. D. Snyder
Department of Orthopedic Surgery, Children's Hospital Boston, Harvard Medical School, Boston, MA 02115, USA

B. D. Snyder (✉)
Orthopedic Biomechanics Laboratory, Beth Israel Deaconess Medical Center, 330 Brookline Avenue, RN115, Boston, MA 02215, USA
e-mail: bsnyder@bidmc.harvard.edu

The skeleton is the third most common site of metastatic cancer, and one-third to half of all cancers metastasize to bone [1]. There are no proven methods for predicting pathologic fractures in patients with skeletal metastasis [2]. While most clinicians assume that bone mineral density (BMD) is the "best" predictor of fracture risk, noninvasive measurement of BMD by dual-energy X-ray absorptiometry (DXA) or quantitative computed tomography (QCT) provides only a surrogate measure of the strength of the affected bone. The prevention of fractures due to skeletal metastasis depends on objective criteria to evaluate changes in bone

structure that reflect the interaction of the metastatic cancer with the host bone. The risk that a bone will fracture through a metastatic lesion depends on the reduction in the load-bearing capacity of the bone induced by the cancer and the loads applied to the bone. From the mechanics of structures, the load-bearing capacity of a bone affected by metastatic cancer depends on the shape and cross-sectional geometry of that bone in addition to its material properties [2–9]. The increased fragility associated with skeletal metastasis suggests that the strength of the bone tissue adjacent to the metastatic lesion is degraded and/or the stresses generated within the bone during loading are increased due to changes in bone geometry [10]. Therefore, any method that assesses fracture risk must be able to measure both changes in the bone tissue material properties and the bone geometry induced by the cancer. As bone tissue material and cancellous bone microstructure are directly affected by osteoclast and osteoblast activity in response to local and systemic cytokines, growth factors, and hormones regardless of the underlying pathology, our hypothesis is that cancellous bone (normal or pathologic) follows the same analytic relationships between BMD and stiffness that have been previously derived for normal and osteoporotic bone [6, 7, 11–18]. However, to the best of our knowledge, this hypothesis has never been validated for metastatic cancer bone tissue. Therefore, the primary aim of this study was to test the hypothesis that a single analytic relationship can predict the strength and stiffness of normal and pathologic cancellous bone affected by osteoporosis or metastatic cancer, where the independent variables were the BMD and bone volume fraction (BV/TV) measured noninvasively by QCT. To accomplish this aim, normal, osteoporotic, and metastatic cancer cancellous bone specimens were imaged using micro-QCT and then tested mechanically by uniaxial compression. Nanoindentation and backscatter emission (BSE) imaging were also performed on the specimens to measure the bone tissue micromechanical properties and bone tissue mineral content. Cancellous bone specimens were then modeled analytically as rigid, open-celled foam [19], where the strength and stiffness of the bone were assumed to be a function of BMD (ρ_{TISSUE}, g cm^{-3}), which reflected the contribution of the mineral and organic matrix to the bone tissue material properties and BV/TV (%), which reflected the contribution of the trabecular microstructure to the continuum level and mechanical properties of cancellous bone [20, 21].

Since cancer metastatic to bone changes the trabecular structure [22] and introduces inhomogeneities that make it difficult to obtain consistent cancellous bone samples required to measure the material properties of pathologic bone specimens that we intended to measure, a secondary aim was to develop a method to determine the dependence of the mechanical properties of structurally inhomogeneous bone specimens affected by metastatic cancer, osteoporosis, or both on BMD and trabecular microstructure. To this end, we used a mechanical testing and data acquisition device previously validated by us [23, 24] that incorporated stepwise axial compression in combination with time-lapsed micro-computed tomographic (μCT) imaging to study the three-dimensional (3D) failure behavior of cellular solids [25]. From structural mechanics, we adapted Castigliano's second theorem [26], which states when an axial force, F, is applied to a series of beams comprising a structure, the total deformation of that structure (δ) is given by the sum of individual beam element deformations:

$$\delta = \sum F\left(\frac{L_i}{E_i A_i}\right) \tag{1}$$

where E_iA_i/L_i is the axial stiffness for each beam element. In this study, we considered each bone specimen to be comprised of a series of stacked, transaxial bone segments of variable stiffness. Since the force applied to the bone specimen was known and the axial displacement for each transaxial segment through the bone specimen was measured after each stepwise force using the time-lapsed μCT imaging system, it was possible to calculate E_i for each transaxial bone segment. E_i was then related to BMD and trabecular microstructure measured on the corresponding transaxial μCT image through the bone specimen. From this analysis it was apparent that the least rigid segment(s) of bone comprising the specimen governed most of the mechanical behavior of the entire specimen.

Materials and Methods

Specimen Preparation

After obtaining institutional review board approval and informed consent from patients with skeletal metastasis, seven females (36–75 years) and eight males (42–83 years), mean age 68 ± 15 years, underwent excisional biopsy of metastatic prostate, breast, lung, ovarian, or colon cancer from the spine or proximal femur at surgery for fracture treatment or at autopsy. A total of 41 cylindrical cancer specimens were cored from the excised bones (Table 1). The specimens were cored along the predominant trabecular orientation (assessed via contact radiography) out of a precut block of the excised bone using a diamond coring tool (Starlite Industries, Rosemont, PA) while completely submerged in 0.9% saline solution. Once cored, both ends of all specimens were cut perpendicular to the longitudinal axis of the specimen between two parallel diamond wafering blades running on a low-speed saw (Isomet; Buehler, Lake Bluff, IL) following previously described protocols [23, 24]. The specimens were cored and cut using a 2:1 ratio

Table 1 Distribution of cancer types along with number of donors and specimens per cancer type

Cancer type	Donors (n)	Specimens (n)
Ovarian	2	3
Lung	4	7
Prostate	4	19
Breast	4	9
Colon	1	3

(diameter 5.40 ± 0.31 mm, height 10.31 ± 0.28 mm) between length and diameter [27].

Additionally, 96 noncancer specimens (diameter 5.53 ± 0.26 mm, height 10.44 ± 0.21 mm) were cored from 43 age- ($P = 0.64$) and site-matched cadaver bones (21 females [26–85 years], 22 males [23–93 years], mean age 65 ± 17 years) employing identical procedures as above. Noncancer specimens were divided between normal and osteoporotic groups. As no patient information regarding the skeletal health of the cadavers was available, areal BMD (aBMD, g cm^{-2}) was measured for all noncancer specimens and compared with site-specific normative aBMD cut-off values for osteoporosis in male and female representatives from the National Health and Nutrition Examination Survey (NHANES) and Hologic (Waltham, MA) data set [28] (female femoral neck aBMD cut-off = 0.600 g cm^{-2}, lumbar spine aBMD cut-off = 0.840 g cm^{-2}; male femoral neck aBMD cut-off = 0.590 g cm^{-2}, lumbar spine aBMD cut-off = 0.816 g cm^{-2}). Specimens that presented with aBMD values less than the cut-off normative data for their respective sex and site were considered osteoporotic ($n = 35$), and the remaining specimens were considered normal ($n = 61$).

Specimens underwent cleaning via sonic agitation (Fisher Scientific, Hampton, NH) while suspended in water for 20 minutes, followed by centrifugal removal of excess water and marrow at 9G for 15 minutes. The average mass (m, g) and physical dimensions of each specimen were measured (average of three measurements per case) using precision balance and calipers. Additionally, bone tissue volume (V_{BONE}, mm^3) of each specimen was measured via pycnometry (Accupyc 1330; Micromeritics, Norcross, GA). Wet bone tissue density (ρ_{TISSUE}, g cm^{-3}) was then calculated as the result of the average mass (m) divided by V_{BONE}.

Specimens underwent μCT imaging and mechanical testing. All tested specimens were sectioned in half axially. One-half of all cancer specimens were used to confirm the presence of skeletal metastasis histologically. The other half of all specimens were prepared for BSE microscopy and nanoindentation. To that end, specimens were dehydrated in ethyl alcohol with increasing concentrations of 70%, 80%, 90%, and 100%. Dried specimens were embedded in low-viscosity epoxy resin (Epo-thin, Buehler) and sanded using silicon carbide abrasive paper of decreasing particle size (600, 800, and 1,200 grit) under irrigation to expose the bony surface. This surface was further polished with alumina suspension (Buehler) with 0.05 μm particle size. The last polishing step was on plain microcloth under deionized water, followed by ultrasonic cleaning to remove surface debris.

Nanoindentation

We obtained bone tissue material properties by means of nanoindentation using a Triboindenter with a Berkovich indenter (Hysitron, Minneapolis, MN). This fully automated hardness testing system makes small indentations at precise positions on a specimen surface while continuously monitoring the loads and displacements of the indenter. The apparatus is enclosed in an insulated cabinet to provide thermal stability and is suspended on an antivibration table to isolate it from external vibrations. The Oliver–Pharr method was used to determine the indentation modulus, hardness, and indenter area function [29, 30]. Measurements of load and displacement were used to determine contact stiffness, and the reduced modulus was determined from the contact stiffness. The elastic properties of the diamond indenter tip, v_{tip} and E_{tip}, are 0.07 and 1,140 GPa, respectively.

Each nanoindentation test was conducted to a maximum load of 6 mN at a constant loading rate of 400 mN/second. The indentation procedure included a linear loading part 15 seconds long, a holding period at maximum load 10 seconds long, and a linear unloading part 15 seconds long. For calculation of elastic properties, 50–95% of the unloading curves was used. Five target areas were selected in each specimen. In each target area, six indents were performed for a total of 30 indents per specimen. The target areas were selected in the trabecular islands or junctions immediately adjacent to the sites of trabecular fracture from conventional mechanical testing.

BSE Imaging

BSE imaging was performed using the XL30 scanning electron microscope (SEM; Philips/FEI, Eindhoven, The Netherlands) with a BSE detector (Philips/FEI). The signal was first calibrated using C ($Z = 6$) and A1 ($Z = 13$), and then the settings were changed to increase the contrast of the bone signal ($Z \pm 10$). During the acquisition session, we controlled the drift of the signal using SiO_2 as a standard (only for slight adjustments) with beam intensity of 20 kV. Digital images were collected at 100× magnification with each file measuring 2×1.5 mm. Images were saved as TIFF files (645×484 pixels, pixel size = 3.00 μm), and adjacent images were obtained on each block.

BSE-generated images were analyzed for the distribution of gray levels, using the Quantimet 500IW system for Image Analysis and Image Processing from Leica (Cambridge, UK). In order to determine the bone mineralization profiles, which are known to vary with age, therapy, and disease, images were segmented into 50 equal bins of increasing intensity (gray levels); the first part of the histograms represents the least mineralized bone (dark gray areas), and the second part contains the distribution of the gray levels corresponding to the most heavily mineralized bone (white areas). The statistical parameters of the histograms—mean, weighted average (BSE-WA), standard deviation, median, mode, skewness, kurtosis, and logit—were determined. In order to estimate the shift to higher mineralization (or lower mineralization), which is a function of the disease, the whole mineralization profiles of the five groups were compared using the logit function: logit = ln[(proportion < 150/proportion > 150)].

Mechanical Testing

A previously described and validated mechanical testing and data acquisition device was employed for this study [23, 24]. This method incorporates stepwise microcompression in combination with time-lapsed μCT to study the 3D failure behavior of cellular solids [25]. Prior to testing, brass end caps (9 mm diameter, 1.2 mm thickness) were glued with cyanoacrylate (American Glue, Taylor, MI) to both ends of the specimens. This reduced end artifact [31] by providing support to the free ends of trabeculae at either end of the specimen. All specimens were preconditioned to eliminate the nonlinear "toe region" [25, 27, 32] at a strain rate of 0.005 s^{-1} for seven cycles. Specimens were transferred to the μCT scanner to image the trabecular architecture in the undeformed state (0% strain), then mounted in the mechanical testing device and subjected to a monocyclic nominal strain of 2% at a strain rate of 0.01 s^{-1}. Sequential time-lapsed images were acquired after application of 4%, 8%, 12%, 16%, and 20% nominal strain. The specimen was allowed to relax for 20 minutes after each incremental strain step to allow for stress relaxation before imaging.

The discrete stepwise mechanical data for each specimen were reconstructed as described previously [24]. Due to the discontinuous nature of the stepwise testing method and the stress relaxation occurring in the specimen between two measurement segments, the stepwise stress–strain graphs consisted of six discontinuous sections between the seven strain steps from 0% to 20% strain. In order to again introduce continuity in the graphs, straight lines were added to the discontinuous regions [33]. Modulus of elasticity (E, N mm^{-2}) in addition to yield strain (ε_Y, mm/mm) and strength (σ_Y, N mm^{-2}), representing intrinsic properties, were reported for the study. Modulus of elasticity was assessed by measuring the slope of the elastic region of the stress–strain curve, and yield strength was assessed as the point where the stress–strain curve ceased to be linear. Yield point was within the first compression step for all specimens and was calculated using the 0.2% offset method. Specimens remained wet during testing with the humidity sealed within the microcompression device. This was verified upon retrieval of wet specimens at the end of the testing periods.

μCT Imaging

Sequential transaxial images were generated using the μCT 20 system (Scanco Medical, Bassersdorf, Switzerland) [34]. Measurements were stored in 3D image arrays with isotropic voxel sizes of 30 μm at 70 kVp tube voltage and 250 ms integration time. A 3D gaussian filter ($\sigma = 1.2$) with a limited, finite filter support (2) was used to suppress the noise in the volumes. These images were segmented to separate bone from background using an iterative thresholding procedure. A component labeling algorithm was applied to these images in order to keep only the largest connected bone component and to remove small particles arising from noise and artifacts.

Each specimen's intact μCT image was divided along the longitudinal axis into 10 subregions of equal height. For each of these subregions, as well as for the whole specimen, direct 3D indices were computed [35]: BV/TV, bone surface density (BS/TV), specific bone surface (BS/BV), structure model index (SMI), trabecular number (Tb.N), trabecular thickness (Tb.Th), fabric tensor Eigen values (H_1–H_3), degree of anisotropy (DA = H_1/H_3), and connectivity density (Conn.D). The subregion with the minimum BV/TV (BV/TV_{MIN}) was identified. Specimens were divided into 10 subregions only to avoid boundary artifacts in the calculations of microstructural indices. Morphometric indices were calculated for the entire specimen and then averaged out over each subregion using a masking procedure (IPL, Scanco Medical). Apparent BMD (volumetric BMD, g/cm^3) was calculated as the product of the bone mineral tissue density (ρ_{TISSUE}, g/cm^3) measured gravimetrically and BV/TV_{AVG} measured by μCT.

The sequential 3D images of each compression step were combined into an animation to illustrate the mode and location of failure for each specimen. For this purpose, the 3D images were initially aligned relative to the bottom end of the specimen, which was fixed during the experiment. Each aligned 3D data set was then visualized under the same conditions (orientation, light settings) using an extended Marching Cubes algorithm [36]. The resulting images were turned into an animation to visualize the region(s) where most of the specimen deformation occurred (Fig. 1). The

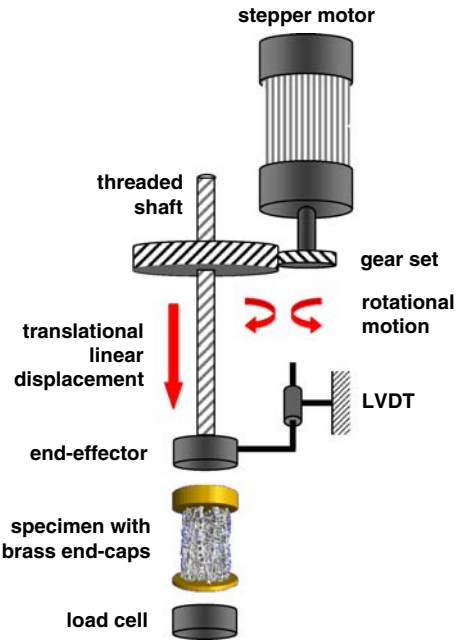

Fig. 1 **a** Schematic of the screw-driven mechanical testing and data acquisition system that translates the rotation of a stepper motor into a controlled, incremental compressive displacement. **b** When the specimen is transferred from the load frame to the μCT for imaging, the displacement applied to the specimen by the actuator is maintained by a custom jig. By sequentially coupling μCT imaging after application of incremental displacement, the failure behavior of the trabecular microstructure is visualized directly. LVDT: linear variable differential transformer

deformation of the subregion with the minimum BV/TV relative to the other subregions comprising the specimen (including the deformation of individual trabeculae) was tracked during sequential compression steps to identify the weakest (least rigid) subregion of the specimen.

Data Analysis

The continuous data were tested for normality using the Kolmogorov-Smirnov test. A power analysis indicated that the sample sizes of cancer ($n = 41$) and noncancer ($n = 96$) specimens provided 80% power to measure the correlation between bone tissue and structural properties and measures of bone strength with a 95% confidence interval (CI) around a moderate Pearson correlation coefficient of 0.60 (nQuery Advisor, version 6.0; Statistical Solutions, Saugus, MA). Multivariable analysis was performed using a linear mixed model strategy, which tests the effects of tissue type (cancer, normal, osteoporosis) and site (spine, proximal femur, distal femur) while controlling for density and bone volume fraction as covariates in the model on E and σ_Y [37]. Multiple specimens from the same donor were handled using a compound symmetry covariance structure, which produced excellent fit to the data as judged by Schwarz's Bayesian criterion [38]. As part of this methodology, statistical significance between tissue types and sites was evaluated using *F*-tests with multiple comparisons according to the Bonferroni procedure to minimize the risk of false-positive results (Type I errors). Rather than using empirically derived regression models that best fit the experimental data, we used a simple regression model of the general form $y = m\ x\ z + b$ (m = slope and b = y-intercept, x and z independent variables, and y dependent variable), based on the theory that cancellous bone can be analytically modeled as an element comprised of a series of breakable subelements to predict E and σ_Y as functions of ρ_{TISSUE}, BV/TV_{AVG}, BV/TV_{MIN}, or vBMD [19, 39].

Since the effective length to width ratio governs the structural behavior of a column, the ratio of effective trabecular length oriented in the principal trabecular direction to mean trabecular thickness was formed to evaluate whether the microstructure of the trabeculae accounted for the variation in BV/TV_{AVG} and BV/TV_{MIN} and further explained the dependence of E and σ_Y on bone volume fraction [40]. The coefficient of determination (R^2) was used as the criterion to compare the different regression models. Our strategy was based on the Fisher r-to-z transformation with a back-transformation of the bounds to produce a 95% CI for the difference between the correlations being compared. This strategy includes the 95% CI and Z test with a two-sided *P* value to test for differences between the correlations [41, 42]. The slopes for the different regression models were compared using generalized estimating equations (GEEs) with the appropriate Wald test for comparing slopes between groups (analogous to analysis of covariance where BV/TV and vBMD and slenderness ratio are treated as covariates).

The SPSS statistical package (version 15.0; SPSS, Inc., Chicago, IL) was used for data analysis. All reported *P* values are two-tailed, with $P < 0.05$ considered statistically significant.

Results

BSE results demonstrated that cancer specimens were hypomineralized in comparison to normal and osteoporotic noncancer specimens (Table 2): The average ρ_{TISSUE} of cancer specimens was 11% lower than that of normal and osteoporotic noncancer specimens ($P < 0.001$); the BSE-WA mineral content of the cancer specimens was 19% and 15% lower than the normal and osteoporotic noncancer specimens, respectively ($P < 0.001$). Additionally, the mineralized tissue comprising the cancer specimens was 50% less hard (H) and less rigid (E_{NANO}) than the normal and osteoporotic noncancer specimens ($P < 0.001$).

Table 2 Material and structural properties for cancer and noncancer specimens (mean ± standard deviation)

Variable	Unit	Metastatic cancer ($n = 41$)	Normal ($n = 61$)	Osteoporosis ($n = 35$)
Tissue density (ρ_{TISSUE}), pycnometry	g cm^{-3}	1.68 ± 0.22*	1.82 ± 0.12	1.81 ± 0.11
Average bone volume fraction (BV/TV_{AVG}), μCT	%	24.29 ± 12.26*	36.46 ± 15.38	25.03 ± 6.22*
Gray level weighted average (BSE-WA), BSE	–	114.82 ± 15.75*	142.91 ± 13.84	135.36 ± 12.14
Hardness (H), nanoindentation	GPa	0.24 ± 0.03*	0.52 ± 0.09	0.47 ± 0.08
Tissue elastic modulus (E_{NANO}), nanoindentation	GPa	0.22 ± 0.03*	0.47 ± 0.07	0.42 ± 0.07
Modulus of elasticity (E), mechanical testing	MPa	201.5 ± 59.68*	356.2 ± 89.7	189.9 ± 95.4*
Yield strength (σ_Y), mechanical testing	MPa	40.4 ± 10.1*	100.5 ± 21.8	40.5 ± 22.4*

* $P < 0.05$, where the reported values for the metastatic cancer and osteoporosis groups are different from normal

The bone volume fraction of the cancer specimens was 33% lower than that of the normal specimens ($P = 0.001$) and not different from that of the osteoporotic specimens ($P = 0.45$). Consistent with the pathophysiology of osteoporosis, which affects trabecular structure but not bone tissue mineralization [43, 44], BV/TV_{AVG} of the osteoporotic specimens was 31% lower than that of the normal noncancer specimens ($P < 0.01$) but ρ_{TISSUE} ($P = 0.65$), BSE mineral content ($P = 0.24$), H, and E_{NANO} were not different between the osteoporotic and normal noncancer specimens ($P > 0.05$) (Table 2).

Sequential μCT images acquired after each incremental stepwise application of compressive strain demonstrated that the least rigid segment of the specimen where the most deformation occurred was at the subregion with the minimum BV/TV (Fig. 2).

A multivariate, linear, mixed model tested the effects of tissue type (cancer, normal, osteoporosis) and anatomic site (spine, proximal femur, distal femur) while controlling for ρ_{TISSUE} and for BV/TV as covariates. Only BV/TV and anatomic site were independently predictive of the mechanical properties E and σ_Y ($P < 0.001$). While three specimen groups were distinguished—normal, osteoporotic, and metastatic cancer—linear regression analyses were performed on the cancer and noncancer specimens, combining the normal and osteoporotic noncancer specimens together as parts of the same continuum [11], and on all the specimens (cancer and noncancer combined) to identify single analytic relationships (Table 3). ρ_{TISSUE} was poorly predictive of either E ($R^2 = 0.13$) or σ_Y ($R^2 = 0.11$) when considered as the independent variable in the linear regression analysis. In comparison, the variation in BV/TV_{AVG} accounted for 79% and 78% of the variation in E and σ_Y, respectively, for all specimens combined regardless of pathology or skeletal site. However, the variation in BV/TV_{MIN} accounted for 84% of the variation in E (Fig. 3a) and 83% of the variation in σ_Y (Fig. 3b) for all specimens combined regardless of pathology or skeletal site.

Using Fisher's Z-transformation test, the coefficients of determination for the linear regressions where E and σ_Y were dependent variables and BV/TV_{MIN} was the independent variable were significantly better than the linear regressions where BV/TV_{AVG} for the entire specimen was the independent variable ($P < 0.01$) (Table 3). This implies that the least rigid segment through the bone specimen where most of the deformation occurs is identified by that cross section through the specimen with the minimum bone volume fraction. However, BV/TV_{AVG} is correlated with BV/TV_{MIN} for all specimens ($R^2 = 0.94$, $P < 0.01$).

vBMD, calculated as the product of ρ_{TISSUE} and BV/TV_{AVG}, explained 85% of the variation in E (Fig. 3c) and 84% of the variation in σ_Y (Fig. 3d) for all specimens combined regardless of pathology or skeletal site. Additionally, for the linear regressions fit separately to the cancer and noncancer specimens, the slopes and y-intercepts were not statistically different between the specimen groups for any of the independent variables evaluated—BV/TV_{AVG}, $P = 0.27$; BV/TV_{MIN}, $P = 0.69$; and vBMD, $P = 0.44$—supporting the hypothesis that the compressive mechanical properties of normal and pathologic bone affected by osteoporosis and/or metastatic cancer are well represented by a single analytic function that reflects the trabecular microstructure. The least rigid cross section through the bone specimen with the minimum BV/TV dictates the mechanical behavior of the entire bone specimen independent of skeletal site or bone pathology. Even though metastatic cancer affects the mineralization, hardness, and stiffness of cancellous bone tissue, this effect is evident primarily at the material level and has less impact on the macroscopic mechanical properties of the entire bone specimen.

Discussion

Osteoporosis and metastatic cancer affect millions of patients (often both in the same patient), and pathologic fracture is a common complication. Modeling human

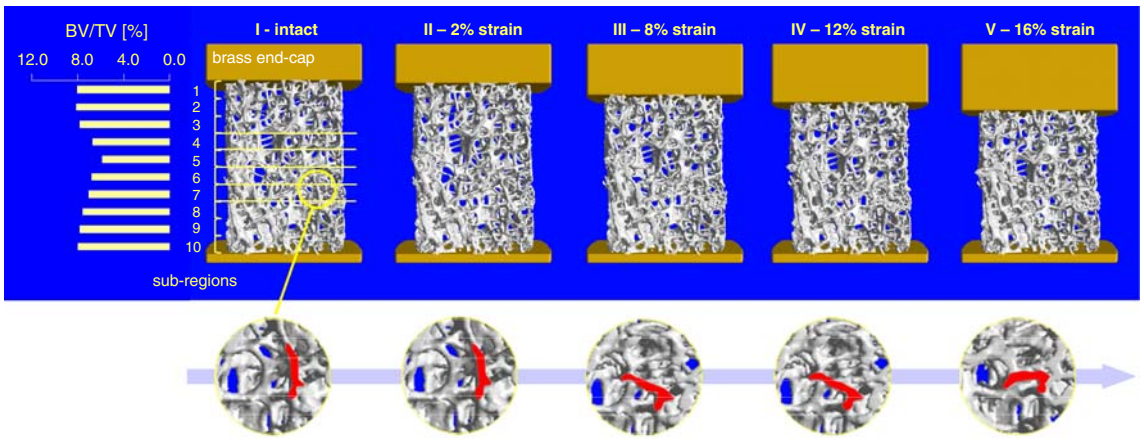

Fig. 2 Specimen (normal specimen shown here) is subdivided into 10 equal-sized transaxial segments (superimposed onto the 3D image of the entire specimen). The relative BV/TV value for each segment is demonstrated by the bar graph. Frames I–V portray the progressive deformation of the trabecular microstructure for the entire specimen. Most of the deformation occurs at the segments with the lowest BV/TV values (segments 4–7). The predominant mode of failure appears to be bending and/or buckling of individual trabeculae. While our results are based on uniaxial compression tests, failure of trabeculae by bending is an important mode of failure even when cancellous bone is subjected to torsion or tension [33, 81, 82]. A (red) representative trabecula (randomly selected from trabeculae that can be easily identified and highlighted in all images) in the magnified image sequence demonstrates the bending of an individual trabecula in response to progressive displacement

Table 3 Mechanical properties of combined cancer and noncancer bone specimens expressed as function of ρ_{TISSUE}, BV/TV_{AVG}, BV/TV_{MIN}, or vBMD

Dependent variable	Equation	R^2
E	$E = 240 \cdot \rho_{TISSUE} - 202$	0.13
	$E = 889 \cdot BV/TV_{AVG} + 5.32$	0.79
	$E = 1{,}050 \cdot BV/TV_{MIN} + 22.3$	0.84
	$E = 1{,}060 \cdot vBMD + 21.0$	0.85
σ_Y	$\sigma_Y = 7.6 \cdot \rho_{TISSUE} - 8$	0.11
	$\sigma_Y = 30.0 \cdot BV/TV_{AVG} - 1.98$	0.78
	$\sigma_Y = 35.6 \cdot BV/TV_{MIN} - 1.4$	0.83
	$\sigma_Y = 36.5 \cdot vBMD - 1.5$	0.84

Models using BV/TV_{MIN} as the independent variable predicted E and σ_Y significantly better ($P < 0.01$) than models using BV/TV_{AVG}, confirming that the least rigid segment of the specimen identified as that with the BV/TV_{MIN} accounted for most of the mechanical behavior of the entire specimen. Addition of ρ_{TISSUE} to the regression model did not make a significant contribution to the predictive power of the models for E or σ_Y. Therefore, regression models where $vBMD = \rho_{TISSUE} \cdot BV/TV_{AVG}$ was the independent variable were not different from regression models where only BV/TV_{MIN} was the independent variable ($P = 0.23$ for E and $P = 0.78$ for σ_Y)

cancellous bone as rigid porous foam, we demonstrated that the cross section through the bone with the minimum bone volume fraction governed the mechanical behavior of the entire specimen for normal, osteoporotic, and metastatic cancer to bone. Surprisingly, bone tissue mineral density alone was not a strong indicator of the macroscopic mechanical behavior of cancellous bone. This result supports the hypothesis that the strength and stiffness of normal and pathologic cancellous bone affected by osteoporosis or metastatic cancer can be predicted using a unified relationship where vBMD or BV/TV measured by QCT is the independent variable. This work establishes the supremacy of bone structure over tissue-level material properties when accounting for the macroscopic, continuum-level behavior of cancellous bone. The unified relationships derived in this work suggest that the net response of cells responsible for making and destroying bone to modifiers of their activity are reflected by changes in the trabecular structure and bone volume fraction.

Since the cells that form and destroy bone are responsible for altering the bone structural and material properties, we hypothesized that, using measures of bone tissue mineralization and trabecular structure, a unified relationship could be derived that predicts the mechanical properties of normal and pathologic bone affected by osteoporosis and/or metastatic cancer. As noted by previous authors [45, 46], the inter- and intraspecimen variability in BMD and trabecular structure can be quite large depending on anatomic site and underlying bone pathology. Since the cancellous bone specimens were structurally heterogeneous, we drew an analogy with Castigliano's second theorem for structures and postulated that the least rigid transaxial subregion through the specimen accounted for most of the specimen deformation and therefore dictated the mechanical behavior of the entire specimen. In the present study, the intraspecimen variation for BV/TV ranged 4–63%, with a mean of 24%. While the

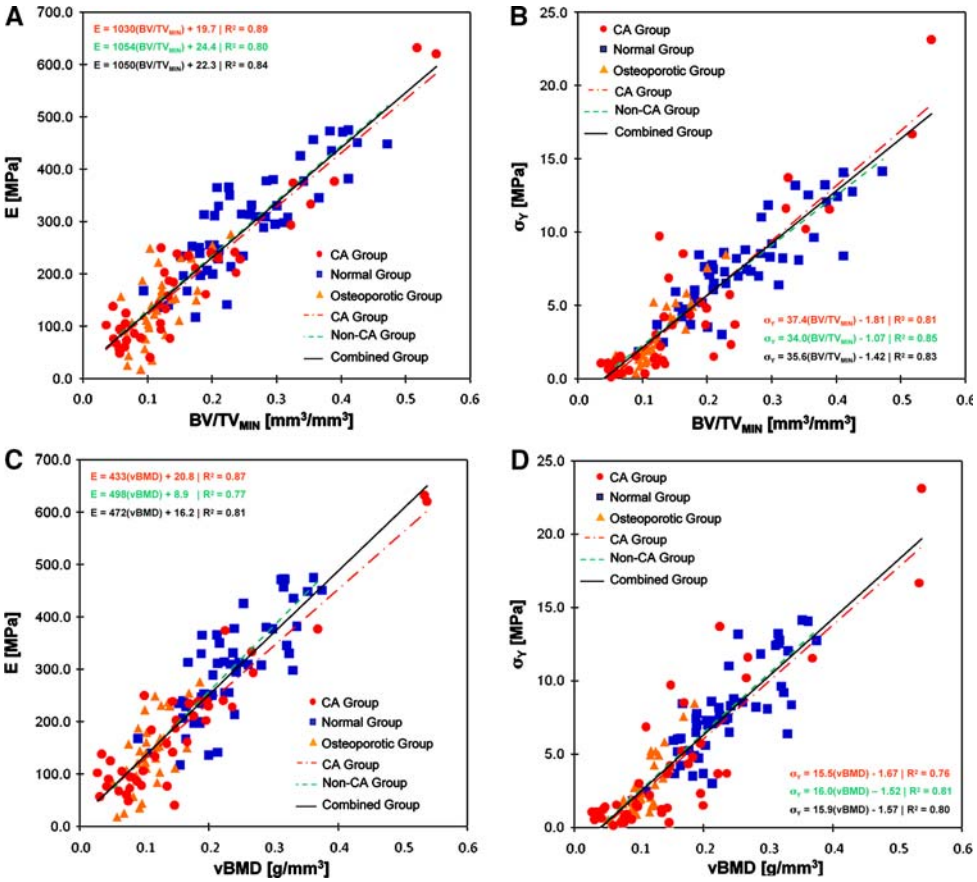

Fig. 3 Linear regression models illustrating that (**a**) modulus of elasticity and (**b**) yield strength of noncancer (normal and osteoporotic) and metastatic cancer cancellous bone specimens are functions of BV/TV_{MIN} regardless of the underlying pathology. Linear regression models illustrating that (**c**) modulus of elasticity and (**d**) yield strength of noncancer (normal and osteoporotic) and metastatic cancer cancellous bone specimens are functions of vBMD regardless of the underlying pathology. Specimen groups: cancer (CA, red), noncancer (green), cancer and noncancer combined (black)

strength and stiffness of normal and pathologic bone specimens of similar BV/TV were variable, this variation was more than bracketed by the range of intra- and inter-specimen variation in BV/TV for all the specimens. In particular, the variation in BV/TV_{MIN} accounted for 84% of the variation in the compressive strength and modulus for all cancellous bone specimens independent of skeletal site or bone pathology, suggesting that the transaxial subregion through the specimen with the minimum BV/TV corresponded to the weakest subregion throughout the specimen with the least axial rigidity.

Even though the metastatic CA specimens were hypomineralized in comparison to the normal and osteoporotic specimens, bone tissue density accounted for <15% of the variation in stiffness and strength of the specimens; the addition of ρ_{TISSUE} explained little additional variation in stiffness or strength not explained by BV/TV alone. For both osteoporosis and metastatic cancer, osteoclast-mediated bone resorption results in a net loss of bone mass and a concomitant change in trabecular structure [47, 48]. Once osteoclasts have resorbed enough bone tissue to create a discontinuity in a trabecular element, that element can no longer support load. As the cross-struts between longitudinally oriented trabeculae become discontinuous, the remaining trabeculae become relatively longer (Fig. 4). Since buckling and bending are the predominant modes of trabecular deformation and failure [49, 50], these changes in trabecular structure influence the mechanical behavior of cancellous bone in disproportion to the corresponding change in mineral mass [40, 51, 52]. The buckling load for a trabecular column is proportional to $EA/(l/r)^2$, where E is the modulus of elasticity of the bone tissue comprising the trabeculae, A is the cross-sectional area of the trabeculae, and l/r is the slenderness ratio, measured as the effective length to width ratio of the trabeculae. We evaluated the extent that trabecular microstructure accounted for the variation in BV/TV and strength by expressing both BV/TV and σ_Y as a function of the inverse square root of the mean trabecular slenderness ratio. Overall, 77% of the variation in BV/TV_{AVG} and nearly 70% of the variation in σ_Y was explained by the mean slenderness ratio for cancer and noncancer specimens combined (Fig. 5a, b). The slope and *y*-intercept for the noncancer group were not statistically different from the combined data ($P = 0.27$); however, the slope and *y*-intercept for the cancer group was statistically different from the combined data ($P < 0.001$). This is partially due to the presence of local lesion in the cancer data where the slenderness ratio of the trabecular network is directly affected in specific areas. As a result, the changes in trabecular structure as a result of unbalanced

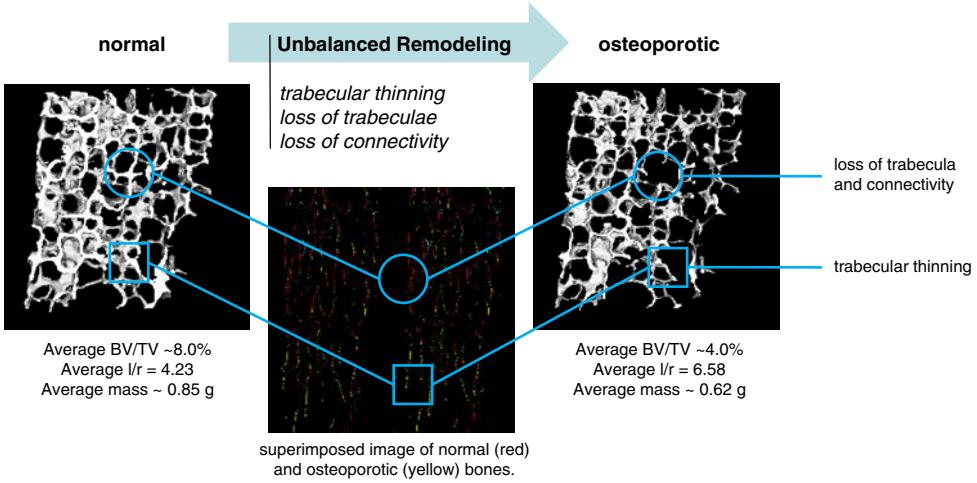

Fig. 4 For both osteoporosis and metastatic cancer, osteoclast-mediated bone resorption results in a net loss of bone mass and a concomitant change in trabecular structure. This example illustrates how changes to the trabecular structure influence the mechanical behavior of cancellous bone in disproportion to the corresponding change in mineral mass. Cancellous bone is comprised of a network of trabecular struts. During unbalanced remodeling, osteoclasts along the surfaces of the trabeculae (red highlight) resorb bone. Once an osteoclast has resorbed enough bone tissue to create a discontinuity, that trabecula can no longer support load. As the transverse trabeculae forming cross-struts between the longitudinally oriented trabeculae become discontinuous, the remaining trabeculae become "functionally" longer. In this example there is a 27% decrease in bone mass but BV/TV has decreased by nearly 50% and the slenderness ratio (l/r) has increased by 56%. These changes in trabecular structure pose a triple threat to the mechanical stability of the cancellous network: Not only are there fewer trabeculae but the remaining trabeculae have become thinner and longer, thereby decreasing their stability to bending and buckling, the primary modes of trabecular failure at the microstructural level, and establishing the supremacy of trabecular structure over mineral mass

bone remodeling pose a triple threat to the mechanical stability of the cancellous network that is disproportionate to the change in mass since not only are there fewer trabeculae but the remaining trabeculae have become thinner and longer, decreasing their stability to bending and buckling in a nonlinear fashion.

Due to the fragility of the metastatic cancer bone specimens, we were unable to test these specimens in tension or torsion. While compression is a common mode of failure, especially in the spine [53, 54], the skeleton is subjected to complex loads that induce tensile, compressive, and shear stresses in bone. Mechanical testing of normal human and bovine cancellous bone specimens has demonstrated that, similar to compression, the shear and tensile properties of cancellous bone depend on BMD [55, 56]. None of these studies compared the influence of ρ_{TISSUE} relative to BV/TV.

Considerable work has been undertaken to understand how alterations in bone density [13], trabecular microstructure [49, 57, 58], bone tissue mineralization [57, 59], organic matrix collagen composition [60, 61], and microcrack propagation [58, 62] affect the micro- and macroscopic mechanical properties of cancellous bone as a result of aging [63, 64] and metabolic bone diseases [65]. Several studies have evaluated bone strength as a function of mineral density [12, 14, 66–68], bone volume fraction [11, 18, 67–69], trabecular microstructure [70, 71], or a combination of these material and microstructural parameters [51, 72, 73] for normal and osteoporotic bone. Even though cancer metastatic to the skeleton affects millions of patients, few studies have measured the mechanical properties of bone tissue affected by metastatic cancer [6, 74]. Kaneko et al. [6] studied the mechanical properties of femora affected by metastatic cancer. They correlated the compressive strength and stiffness of cancer and noncancer specimens extracted from distal femora containing osteolytic lesions with vBMD measured by peripheral QCT. Similar to our study, they found that vBMD accounted for >77% of the mechanical behavior of the cancer and noncancer specimens combined.

The clinical implications of this work are important for developing noninvasive in vivo fracture risk predictions for bones affected by metastatic cancer, osteoporosis, or both using sequential, transaxial CT [4, 9, 75, 76] or magnetic resonance [77–79] images of the involved bones. We have previously applied composite beam theory and structural engineering analysis to sequential, transaxial CT images of bones affected by benign and malignant neoplasms to calculate the load-carrying capacity of the bones and to predict the fracture risk in vivo for children with benign skeletal neoplasms and for women with metastatic breast cancer to the spine [3, 9]. Fracture risk assessments based

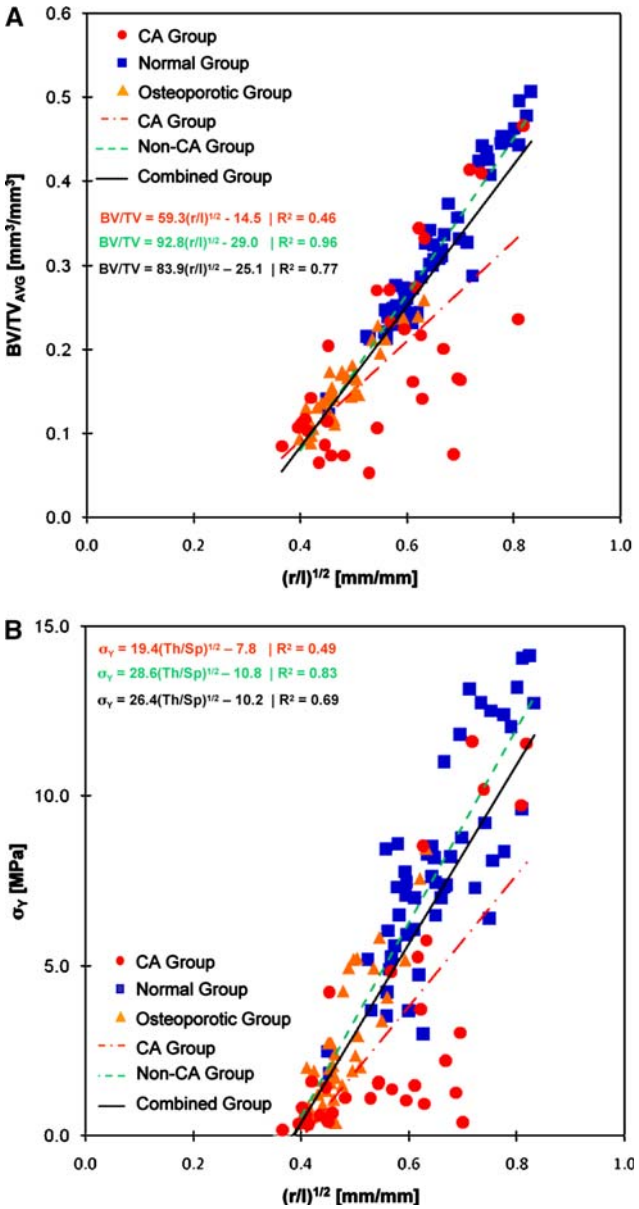

◀ **Fig. 5** BV/TV (**a**) and σ_Y (**b**) plotted as a function of the inverse square root of the slenderness ratio of trabecular elements for each specimen. Specimen groups: cancer (CA, red), noncancer (green), cancer and noncancer combined (black). Overall, 77% of the variation in BV/TV is accounted for by the variation in the inverse square root of the slenderness ratio of the trabeculae. However, for the noncancer specimens, 96% of the variation in BV/TV is explained by the variation in the inverse square root of the slenderness ratio of the trabeculae, but for the cancer specimens only 46% of the variation in BV/TV is explained by the variation in the inverse square root of the slenderness ratio of the trabeculae. This is partially due to the presence of specimens from patients with prostate cancer (with mostly osteoblastic lesions), where for a given bone volume fraction the trabeculae are thicker and shorter than specimens from mostly osteolytic lesions. For the noncancer bone, remodeling is slower and remains coupled under systemic control and the mean changes in trabecular thickness and length are representative of the changes in trabecular microstructure throughout the specimen. In metastatic cancer, malignant cells produce local factors that stimulate osteoclasts to aggressively resorb bone, creating lytic lesions. The bone remodeling process becomes uncoupled; bone formation is suppressed and the lesion cannot be repaired [83]. Unlike osteoporosis, the focal and localized resorption of trabeculae induced by metastatic breast cancer is not captured by the mean changes in trabecular thickness to length measured over the entire specimen

on composite beam theory or patient-specific finite element models developed from 3D CT data sets [80] require constitutive data for each element of the model. The analytic relationships derived in this work provide these data: E and σ_Y can be calculated from vBMD derived from the CT-based X-ray attenuation coefficient corresponding to each element of the model for normal, osteoporotic, or metastatic cancer cancellous bone.

Acknowledgements This study was funded by National Institutes of Health grant CA40211 (to B. D. S.), Susan G. Komen grant BCTR0403271 (to B. D. S.), Swiss National Science Foundation grants FP 620–58097.99 and PP-104317/1 (to R. M.), and a Fulbright Full Grant for Graduate Study and Research Abroad (to A. N.). The authors acknowledge Dr. Marc Grynpas for BSE microscopy imaging, Dr. Zaifeng Fan for nanoindentation, Dr. Andrew Rosenberg for providing histological confirmation of skeletal metastasis in bone specimens, and Dr. Martin Stauber for assistance in image visualization. Additionally, they acknowledge Dr. Evan Snyder from Burnham Institute for Medical Research for reviewing the manuscript and providing helpful comments.

References

1. Michaeli DA, Inoue K, Hayes WC, Hipp JA (1999) Density predicts the activity-dependent failure load of proximal femora with defects. Skeletal Radiol 28:90–95
2. Hipp JA, Springfield DS, Hayes WC (1995) Predicting pathologic fracture risk in the management of metastatic bone defects. Clin Orthop Relat Res 312:120–135
3. Snyder BD, Hauser-Kara DA, Hipp JA, Zurakowski D, Hecht AC, Gebhardt MC (2006) Predicting fracture through benign skeletal lesions with quantitative computed tomography. J Bone Joint Surg Am 88:55–70
4. Hong J, Cabe GD, Tedrow JR, Hipp JA, Snyder BD (2004) Failure of trabecular bone with simulated lytic defects can be predicted non-invasively by structural analysis. J Orthop Res 22:479–486
5. Keyak JH, Kaneko TS, Tehranzadeh J, Skinner HB (2005) Predicting proximal femoral strength using structural engineering models. Clin Orthop Relat Res 437:219–228
6. Kaneko TS, Bell JS, Pejcic MR, Tehranzadeh J, Keyak JH (2004) Mechanical properties, density and quantitative CT scan data of trabecular bone with and without metastases. J Biomech 37: 523–530
7. Kaneko TS, Pejcic MR, Tehranzadeh J, Keyak JH (2003) Relationships between material properties and CT scan data of cortical bone with and without metastatic lesions. Med Eng Phys 25:445–454
8. Bevill G, Eswaran SK, Gupta A, Papadopoulos P, Keaveny TM (2006) Influence of bone volume fraction and architecture on computed large-deformation failure mechanisms in human trabecular bone. Bone 39:1218–1225

9. Whealan KM, Kwak SD, Tedrow JR, Inoue K, Snyder BD (2000) Noninvasive imaging predicts failure load of the spine with simulated osteolytic defects. J Bone Joint Surg Am 82: 1240–1251
10. Hayes WC, Bouxsein ML (1997) Biomechanics of cortical and trabecular bone: implication for assessment of fracture risk. In: Mow VC, Hayes WC (eds) Basic orthopaedic biomechanics. Lippincott-Raven, Philadelphia, pp 69–112
11. Homminga J, McCreadie BR, Weinans H, Huiskes R (2003) The dependence of the elastic properties of osteoporotic cancellous bone on volume fraction and fabric. J Biomech 36:1461–1467
12. Keller TS (1994) Predicting the compressive mechanical behavior of bone. J Biomech 27:1159–1168
13. Carter DR, Hayes WC (1976) Bone compressive strength: the influence of density and strain rate. Science 194:1174–1176
14. Rice JC, Cowin SC, Bowman JA (1988) On the dependence of the elasticity and strength of cancellous bone on apparent density. J Biomech 21:155–168
15. Kowalczyk P (2003) Elastic properties of cancellous bone derived from finite element models of parameterized microstructure cells. J Biomech 36:961–972
16. Kowalczyk P (2006) Orthotropic properties of cancellous bone modelled as parameterized cellular material. Comput Methods Biomech Biomed Eng 9:135–147
17. Bourne BC, van der Meulen MC (2004) Finite element models predict cancellous apparent modulus when tissue modulus is scaled from specimen CT-attenuation. J Biomech 37:613–621
18. Hernandez CJ, Beaupre GS, Keller TS, Carter DR (2001) The influence of bone volume fraction and ash fraction on bone strength and modulus. Bone 29:74–78
19. Gibson LJ (1997) Cellular solids. Cambridge University Press, New York
20. Parfitt A, Drezner M, Glorieux F, Kanis J, Recker R (1987) Bone histomorphometry: standardization of nomenclature, symbols and units. J Bone Miner Res 2:595–610
21. Pattijn V, Van Cleynenbreugel T, Vander Sloten J, Van Audekercke R, Van der Perre G, Wevers M (2001) Structural and radiological parameters for the nondestructive characterization of trabecular bone. Ann Biomed Eng 29:1064–1073
22. Szejnfeld VL, Monier-Faugere MC, Bognar BJ, Ferraz MB, Malluche HH (1997) Systemic osteopenia and mineralization defect in patients with ankylosing spondylitis. J Rheumatol 24:683–688
23. Nazarian A, Muller R (2004) Time-lapsed microstructural imaging of bone failure behavior. J Biomech 37:55–65
24. Nazarian A, Stauber M, Muller R (2005) Design and implementation of a novel mechanical testing system for cellular solids. J Biomed Mater Res B Appl Biomater 73:400–411
25. Muller R, Gerber SC, Hayes WC (1998) Micro-compression: a novel technique for the nondestructive assessment of local bone failure. Technol Health Care 6:433–444
26. Timoshenko S, Goodier JN (1970) Theory of elasticity, 3rd edn. McGraw-Hill, New York
27. Keaveny TM, Borchers RE, Gibson LJ, Hayes WC (1993) Theoretical analysis of the experimental artifact in trabecular bone compressive modulus. J Biomech 26:599–607
28. Richy F, Gourlay ML, Garrett J, Hanson L, Reginster JY (2004) Osteoporosis prevalence in men varies by the normative reference. J Clin Densitom 7:127–133
29. Oliver WC, Pharr GM (1992) An improved technique for determining hardness and elastic modulus using load and displacement sensing indentation experiments. J Mater Res 7(6): 1564–1583
30. Rho J-Y, Tsui TY, Pharr GM (1998) Elastic properties of human cortical and trabecular lamellar bone measured by nanoindentation. Biomaterials 18:1325–1330
31. Keaveny TM, Pinilla TP, Crawford RP, Kopperdahl DL, Lou A (1997) Systematic and random errors in compression testing of trabecular bone. J Orthop Res 15:101–110
32. Keaveny TM, Borchers RE, Gibson LJ, Hayes WC (1993) Trabecular bone modulus and strength can depend on specimen geometry. J Biomech 26:991–1000
33. Nazarian A, Müller R (2004) Time-lapsed microstructural imaging of bone failure behavior. J Biomech 37:55–65
34. Ruegsegger P, Koller B, Muller R (1996) A microtomographic system for the nondestructive evaluation of bone architecture. Calcif Tissue Int 58:24–29
35. Hildebrand T, Laib A, Muller R, Dequeker J, Ruegsegger P (1999) Direct three-dimensional morphometric analysis of human cancellous bone: microstructural data from spine, femur, iliac crest, and calcaneus. J Bone Miner Res 14:1167–1174
36. Lorensen WE, Cline HE (1987) Marching cubes: a high resolution 3D surface construction algorithm. Comput Graph 21:163–169
37. Laird NM, Ware JH (1982) Random-effects models for longitudinal data. Biometrics 38:963–974
38. Schwarz G (1978) Estimating the dimension of a model. Ann Stat 6:461–464
39. Gibson LJ (2005) Biomechanics of cellular solids. J Biomech 38:377–399
40. Snyder BD, Piazza S, Edwards WT, Hayes WC (1993) Role of trabecular morphology in the etiology of age-related vertebral fractures. Calcif Tissue Int 53:S14–S22
41. Meng XW, Rosenthal R, Rubin DB (1992) Comparing correlated correlation coefficients. Quant Methods Psychol 111:172
42. Dunn OJ, Clark V (1969) Correlation coefficients measured on the same individuals. J Am Stat Assoc 64:366–377
43. Lane JM, Nydick M (1999) Osteoporosis: current modes of prevention and treatment. J Am Acad Orthop Surg 7:19–31
44. Riggs BL, Melton LJIII (1986) Involutional osteoporosis. N Engl J Med 314:1676–1686
45. Kim DG, Hunt CA, Zauel R, Fyhrie DP, Yeni YN (2007) The effect of regional variations of the trabecular bone properties on the compressive strength of human vertebral bodies. Ann Biomed Eng 35:1907–1913
46. Cody D, Goldstein S, Flynn M, Brown E (1991) Correlations between vertebral regional bone mineral density (rBMD) and whole bone fracture load. Spine 16:146–154
47. Cummings SR, Black DM, Nevitt MC, Browner W, Cauley J, Ensrud K, Genant HK, Palermo L, Scott J, Vogt TM (1993) Bone density at various sites for prediction of hip fractures. The Study of Osteoporotic Fractures Research Group. Lancet 341:72–75
48. Hui SL, Slemenda CW, Carey MA, Johnston CC Jr (1995) Choosing between predictors of fractures. J Bone Miner Res 10:1816–1822
49. Silva MJ, Gibson LJ (1997) Modeling the mechanical behavior of vertebral trabecular bone: effects of age-related changes in microstructure. Bone 21:191–199
50. Ford CM, Keaveny TM (1996) The dependence of shear failure properties of trabecular bone on apparent density and trabecular orientation. J Biomech 29:1309–1317
51. Goulet R, Goldstein S, Ciarelli M, Kuhn J, Brown M, Feldkamp L (1994) The relationship between the structural and orthogonal compressive properties of trabecular bone. J Biomech 27:375–389
52. Hodgskinson R, Currey JD (1990) The effect of variation in structure on the Young's modulus of cancellous bone: a comparison of human and non-human material. Proc Inst Mech Eng 204:115–121
53. McBroom RJ, Hayes WC, Edwards WT, Goldberg RP, White AA (1985) Prediction of vertebral body compressive fracture using quantitative computed tomography. J Bone Joint Surg Am 67: 1206–1214

54. Silva M, Keaveny T, Hayes W (1997) Load sharing between the shell and centrum in the lumbar vertebral body. Spine 22: 140–150
55. Yeni YN, Dong XN, Fyhrie DP, Les CM (2004) The dependence between the strength and stiffness of cancellous and cortical bone tissue for tension and compression: extension of a unifying principle. Biomed Mater Eng 14:303–310
56. Keaveny TM, Wachtel EF, Zadesky SP, Arramon YP (1999) Application of the Tsai-Wu quadratic multiaxial failure criterion to bovine trabecular bone. J Biomech Eng 121:99–107
57. Currey J (1986) Effects of porosity and mineral content on the Young's modulus of bone. In: European Society of Biomechanics. 5th ESB Conference, Berlin, p 104
58. Yeni Y, Brown C, Wang Z, Norman T (1997) The influence of bone morphology on fracture toughness of the human femur and tibia. Bone 21:453–459
59. Currey JD (1984) Effects of differences in mineralization on the mechanical properties of bone. Philos Trans R Soc Lond B Biol Sci 304:509–518
60. Viguet-Carrin S, Garnero P, Delmas PD (2006) The role of collagen in bone strength. Osteoporos Int 17:319–336
61. Zioupos P, Currey JD, Hamer AJ (1999) The role of collagen in the declining mechanical properties of aging human cortical bone. J Biomed Mater Res 45:108–116
62. Diab T, Vashishth D (2005) Effects of damage morphology on cortical bone fragility. Bone 37:96–102
63. Mayhew PM, Thomas CD, Clement JG, Loveridge N, Beck TJ, Bonfield W, Burgoyne CJ, Reeve J (2005) Relation between age, femoral neck cortical stability, and hip fracture risk. Lancet 366:129–135
64. Wang XF, Duan Y, Beck TJ, Seeman E (2005) Varying contributions of growth and ageing to racial and sex differences in femoral neck structure and strength in old age. Bone 36:978–986
65. Turner CH (2002) Biomechanics of bone: determinants of skeletal fragility and bone quality. Osteoporos Int 13:97–104
66. Carter DR, Hayes WC (1977) The compressive behavior of bone as a two-phase porous structure. J Bone Joint Surg Am 59:954–962
67. Keaveny TM, Wachtel EF, Ford CM, Hayes WC (1994) Differences between the tensile and compressive strengths of bovine tibial trabecular bone depend on modulus. J Biomech 27:1137–1146
68. Hou FJ, Lang SM, Hoshaw SJ, Reimann DA, Fyhrie DP (1998) Human vertebral body apparent and hard tissue stiffness. J Biomech 31:1009–1015
69. Schaffler MB, Burr DB (1988) Stiffness of compact bone: effects of porosity and density. J Biomech 21:13–16
70. Turner CH, Cowin SC, Rho JY, Ashman RB, Rice JC (1990) The fabric dependence of the orthotropic elastic constants of cancellous bone. J Biomech 23:549–561
71. Van Rietbergen B, Odgaard A, Kabel J, Huiskes R (1998) Relationships between bone morphology and bone elastic properties can be accurately quantified using high-resolution computer reconstructions. J Orthop Res 16:23–28
72. Cowin SC (1985) The relationship between the elasticity tensor and the fabric tensor. Mech Mater 4:137–147
73. Kabel J, van Rietbergen B, Odgaard A, Huiskes R (1999) Constitutive relationships of fabric, density, and elastic properties in cancellous bone architecture. Bone 25:481–486
74. Hipp JA, Rosenberg AE, Hayes WC (1992) Mechanical properties of trabecular bone within and adjacent to osseous metastases. J Bone Miner Res 7:1165–1171
75. McBroom RJ, Cheal EJ, Hayes WC (1988) Strength reductions from metastatic cortical defects in long bones. J Orthop Res 6:369–378
76. McBroom RJ, Hayes WC, Edwards WT, Goldberg RP, White AA 3rd (1985) Prediction of vertebral body compressive fracture using quantitative computed tomography. J Bone Joint Surg Am 67:1206–1214
77. Wehrli FW, Saha PK, Gomberg BR, Song HK, Snyder PJ, Benito M, Wright A, Weening R (2002) Role of magnetic resonance for assessing structure and function of trabecular bone. Top Magn Reson Imaging 13:335–355
78. Newitt DC, Majumdar S, van Rietbergen B, von Ingersleben G, Harris ST, Genant HK, Chesnut C, Garnero P, MacDonald B (2002) In vivo assessment of architecture and micro-finite element analysis derived indices of mechanical properties of trabecular bone in the radius. Osteoporos Int 13:6–17
79. Hong J, Hipp JA, Mulkern RV, Jaramillo D, Snyder BD (2000) Magnetic resonance imaging measurements of bone density and cross-sectional geometry. Calcif Tissue Int 66:74–78
80. Crawford RP, Cann CE, Keaveny TM (2003) Finite element models predict in vitro vertebral body compressive strength better than quantitative computed tomography. Bone 33:744–750
81. Nazarian A, Stauber M, Müller R (2005) Design and implementation of a novel mechanical testing system for cellular solids. J Biomed Mater Res B Appl Biomater 73:400–411
82. Michel M, Guo X, Gibson L, McMahon T, Hayes W (1993) Compressive fatigue behavior of bovine trabecular bone. J Biomech 26:453–463
83. Galasko CS (1976) Mechanisms of bone destruction in the development of skeletal metastases. Nature 263:507–508